**ROYAL SOCIETY OF CHEMISTRY**

## PAPER

Check for updates

# Enhanced H$_2$ production at the atomic Ni–Ce interface following methanol steam reforming†

Yaqi Hu,‡[a] Zhong Liang,‡[a] Yabin Zhang,[b] Yaping Du ✪ *[acd] and Hongbo Zhang ✪ *[ac]

Hydrogen production with high efficiency and low CO selectivity in methanol steam reforming (MSR) is of pivotal importance. However, there is limited understanding of the active sites and reaction mechanisms during catalysis. In this study, we maximized the interfacial site, known as the active component in MSR, of Ni–CeO$_x$ by atomically dispersed Ni and Ce over the carbon–nitrogen support to generate the Ni and Ce dual-atomic catalyst (DAC), which achieved 6.5 μmol$_{H_2}$ g$_{cat.}^{-1}$ s$^{-1}$ H$_2$ generation rate and 0.8% CO selectivity at 99.1% methanol conversion at 513 K. The finely dispersed Ni and Ce structure was confirmed by systematic characterization of AC HAADF-STEM and EXAFS. Electron transfer from Ce to Ni was confirmed simultaneously by quasi-*in situ* XPS analysis. Moreover, the reaction mechanism of methanol steam reforming was clarified by combining kinetic studies with isotope-tracing/exchange analysis (*i.e.*, KIEs and steady-state isotopic transient kinetic analysis (SSITKA)), which suggests that the steam reforming consists of two tandem reaction processes: methanol decomposition (MD) and water–gas shift (WGS) reaction, with methanol and water activation at independent active sites (*e.g.*, Ni and oxygen vacancy over CeO$_x$), and that hydrogen generation was primarily determined by both C–H bond rupture and O$_L$–H (O$_L$ represents the lattice oxygen) cleavage within methoxy and hydroxyl groups, respectively, with the catalytic surface mainly covered by CO and methoxy groups. A shift of WGS involvement in hydrogen generation from negligibly influenced to significantly promoted was selectively observed once modifying the reaction from differential conditions to a high methanol conversion regime, and two quantification methods have been established by comparing the molecule ratio between CO and CO$_2$ or H$_2$.

### Broader context

Hydrogen is regarded as a clean energy resource to solve the increasingly serious energy crisis and environmental pollution due to its high energy density and no greenhouse gas emissions during consumption. However, the safe transportation and storage has been an obstacle to its widespread application. Liquid fuel as a hydrogen carrier is a good solution. Methanol is a promising liquid organic hydrogen carrier (LOHC) with a wide range of sources, low price, high hydrogen content and low transportation temperature. Methanol steam reforming (MSR) has a high efficiency in hydrogen production and was widely applied in industry. Currently, the main catalytic systems used are Cu-based non-noble metal catalysts and Pt-based or Pd-based noble metal catalysts. Nevertheless, the poor stability and high price limit their wide application. We constructed an efficient and stable NiCe dual-atomic catalyst containing a large number of atomically dispersed Ni–CeO$_x$ interfacial sites, with high conversion and low CO selectivity in MSR, and confirmed the reaction mechanism of MSR within this catalytic system. Our work will inspire further explorations in the establishment of atomically NiCe active interfacial sites to enhance reaction activity.

[a] Tianjin Key Lab for Rare Earth Materials and Applications, Center for Rare Earth and Inorganic Functional Materials, Smart Sensing Interdisciplinary Science Center, School of Materials Science and Engineering, National Institute for Advanced Materials, Nankai University, Tianjin, 300350, P. R. China. E-mail: ypdu@nankai.edu.cn, hbzhang@nankai.edu.cn

[b] State Key Laboratory of Featured Metal Materials and Life-cycle Safety for Composite Structures, MOE Key Laboratory of New Processing Technology for Nonferrous Metals and Materials, and School of Resources Environment and Materials, Guangxi University, Nanning, 530004, P. R. China

[c] Haihe Laboratory of Sustainable Chemical Transformations, Tianjin, 300350, P. R. China

[d] Key Laboratory of Rare Earths, Chinese Academy of Sciences, Ganzhou, 341119, P. R. China

† Electronic supplementary information (ESI) available. See DOI: https://doi.org/10.1039/d3ey00225j

‡ These authors contributed equally.

# Introduction

Hydrogen is definitely a good energetic resource owing to its high energy content and negligible contamination of the environment. However, it was prohibited from widespread utilization owing to its unstable nature.[1] People keep looking for alternative strategies to replace the traditional method in hydrogen generation, storage and transportation. For example, compared with the high temperature production from fossil fuels, *in situ* generated hydrogen from oxygenated chemicals, such as methanol is more attractive due to the low energy requirement during catalysis,[2–5] which includes methanol steam reforming (MSR), methanol partial oxidation (MPO), methanol oxidative steam reforming (MOSR), and methanol aqueous-phase reforming (MAPR). MSR is the most efficient method with a high $H_2$ gravimetric density of 18.8% and has been widely applied in industry.[5–8]

However, the overall reaction performance of MSR has been influenced by the limited understanding of the reaction mechanism received. Nevertheless, several hypothesized reaction routes have been proposed, which include the dissociative adsorption of methanol followed by subsequent dehydrogenation, and the reaction intermediates vary along with different processes.[9] For example, until now, three different reaction pathways have been proposed and suggest three different reaction intermediates, including $CO^*$,[10–14] $CHOOCH_3^*$[15,16] and $CHOO^*$,[17–20] in which the formate-pathway is mostly accepted. In addition, Peppley[12,13] and Iglesia[14] both suggested that the MSR followed a tandem reaction process with methanol dehydrogenation (MD), followed by water–gas shift (WGS) reactions. Iglesia *et al.* proposed that the elementary step for the dehydrogenation of $CH_3O^*$ is the rate-determining step (RDS) with the WGS reaction as quasi-equilibrated, which was supported by the isotopic and kinetic assessment applied. However, this adjustment might rely on the systems investigated and the reaction conditions applied. WGS will not always be facile with respect to MD or MSR.

With a systematic investigation, it was observed that the interface structure between transition metals and reducible metal oxides within the catalysts plays a vital role in regulating the reaction activity.[11,18,21–26] For example, Li *et al.*[18] developed a method to optimize the surface structure of the commercial $Cu/ZnO/Al_2O_3$ catalyst by manipulating the composition of reducing agents at the activation stage. Due to the existence of adsorbate-induced strong metal–support interactions, the $ZnO_x$ species would constantly migrate to the surface of the metallic $Cu^0$ nanoparticles, forming abundant $Cu–ZnO_x$ interfacial sites. This resulted in the long-term stability, and the catalytic activity of MSR was significantly improved. More interestingly, Köwitsch *et al.*[21] designed $In_3Pd_2$–$InPd/In_2O_3$ nanocomposites with significant amounts of interfaces formed. This was induced by the dynamic reactive metal–support interaction (RMSI) between the intermetallic In–Pd and $In_2O_3$ under the MSR reaction, leading to an unusually high $CO_2$ selectivity of 99% at 573 K. Furthermore, they proposed the participation of oxygen from the reactive $In_xPd_y/In_2O_3$ interface by isotope-labeling. Our recent work also suggests that the interfacial sites are the active component for both WGS[27] and MSR[28] reactions. Therefore, it is crucial to maximize the interfacial sites

that could be achieved by reducing the size of the metal nanoparticles to clusters or even single atoms,[29] and improve the efficiency of metal utilization and control the related side reactions. Specifically, Ma *et al.* synthesized Au layered clusters,[30] isolated Pt atoms ($Pt_1$) and subnanometer Pt clusters ($Pt_n$)[31] decorated α-MoC catalysts to create the interfacial catalytic systems for the ultra-low-temperature WGS reaction, which is the primary side reaction of MSR. The abundant surface hydroxyls of α-MoC provide significant active sites for water dissociation. Owing to the excellent catalytic performance of α-MoC in WGS, they developed a series of good catalysts with atomically dispersed Pt[11] or Ni,[32] which exhibited extraordinary hydrogen production activity in the aqueous-phase methanol reforming. The synergy between Pt or Ni and α-MoC also produces an active interfacial structure for methanol reforming.

Additionally, as described in the literature, the most commonly utilized catalytic system can be classified into non-noble-metal catalysts such as Cu-based catalysts[17,18,33–36] and noble-metal catalysts, for example, Pd-based[36,37] or Pt-based catalysts.[11,38,39] However, the biggest problem with the Cu-based catalysts is the tendency of Cu crystallization and readily sintering at relatively high temperature. As for noble-metal catalysts, although the activities are excellent, the high price is the main obstacle limiting their large-scale application. Therefore, developing efficient non-noble-metal catalytic systems with high reactivity and stability is highly desired but challenging.[40–42]

Collectively, people have devoted many efforts in improving the reactivity of alcohols (methanol and ethanol) steam reforming by: (i) establishing active transition metal–metal oxide interface;[17,18,21,43–48] (ii) constructing active bimetallic-mineral support structure, *etc.*[49–51] Rare earth oxides such as cerium oxide ($CeO_2$) have been confirmed to play an important role in our previous work[27,52] due to the rich oxygen vacancy ($O_V$) and unique electronic structures. Therefore, the atomically dispersed $CeO_x$ would help water activation during catalysis. Here, we designed an atomically dispersed Ni–$CeO_x$ interfacial catalyst by the stepwise selective decoration of isolated Ni and Ce to the carbon–nitrogen support, which would certainly help to establish an atomically bonded interfacial structure (*i.e.*, Ni–$CeO_x$ DAC).[53] During the catalytic evaluation, this specific active site does facilitate the MSR to some extent. The enhanced overall dehydrogenation rate was determined at 6.5 $\mu mol_{H_2}\ g_{cat.}^{-1}\ s^{-1}$ at 513 K with limited CO generated (∼0.8%) at 99.1% methanol conversion. With this simple reaction model established, the overall reaction mechanism of MSR was tentatively probed by a combination of kinetic studies, isotope-tracing experiments, as well as steady-state isotopic transient kinetic analysis (SSITKA), in which hydrogen formation was proved to be determined by a combination of C–H bond rupture within $CH_3O^*$ and $O_L$–H ($O_L$: lattice oxygen) bond cleavage (kinetically relevant) during MSR, respectively.

# Results and discussion

### Synthesis and structural characterization of the NiCe/CN DAC

To synthesize the Ni and Ce dual-atomic catalyst (NiCe/CN DAC), atomic Ni and Ce centers were deposited to the carbon

nitride (CN) support following an incipient wetness impregnation method (detailed preparation procedures presented in Experimental section). Powder X-ray diffraction (XRD) was employed to investigate the structure of the as-prepared dual and single atom catalysts. XRD patterns (Fig. S1, ESI†) show only one peak corresponding to nitrogen-doped carbon and no diffraction peaks attributed to metal in all catalysts. The morphology of the fresh NiCe/CN DAC was investigated by the transmission electron microscope (TEM). Fig. 1a(i) and Fig. S2(i) (ESI†) show the morphology of the thin rolled nanosheets. As determined by the Brunauer–Emmett–Teller (BET) method, the specific surface area of NiCe/CN DAC was 43.1 m$^2$ g$^{-1}$ (Fig. S3a, ESI†). Pores with an average size of $\sim$6.9 nm were also revealed from the gas adsorption isotherms (Fig. S3b, ESI†). Similar to NiCe/CN DAC, the specific surface area of Ni/CN SAC was 46.9 m$^2$ g$^{-1}$ and the pores of Ni/CN SAC had an average size of $\sim$6.8 nm (Fig. S3c and d, ESI†), suggesting that the addition of

different metals has little effect on the morphology and pore structure of the support. In addition, Ni/CeO$_2$ prepared by the incipient wetness impregnation method has a significantly different pore structure, with a specific surface area of 65.5 m$^2$ g$^{-1}$ and pores with an average diameter of $\sim$11.1 nm (Fig. S3e and f, ESI†).

The elemental distribution of the NiCe/CN DAC was ascertained by the energy-dispersive spectroscopy (EDS) mapping. Fig. 1a(ii, iii) and Fig. S2(iii, iv) (ESI†) show that the signals of the Ni and Ce elements are uniformly distributed throughout the CN support, confirming the high dispersion of Ni and Ce centers within NiCe/CN DAC. To further confirm that, Aberration-corrected high-angle annular dark field-scanning transmission electron microscopy (AC HAADF-STEM) was conducted. The isolated bright spots can be distinguishably identified, corresponding to monodispersed Ni and Ce centers with an average diameter of 0.27 nm (Fig. 1b, eqn (5)). X-ray absorption spectroscopy (XAS) was also performed to further
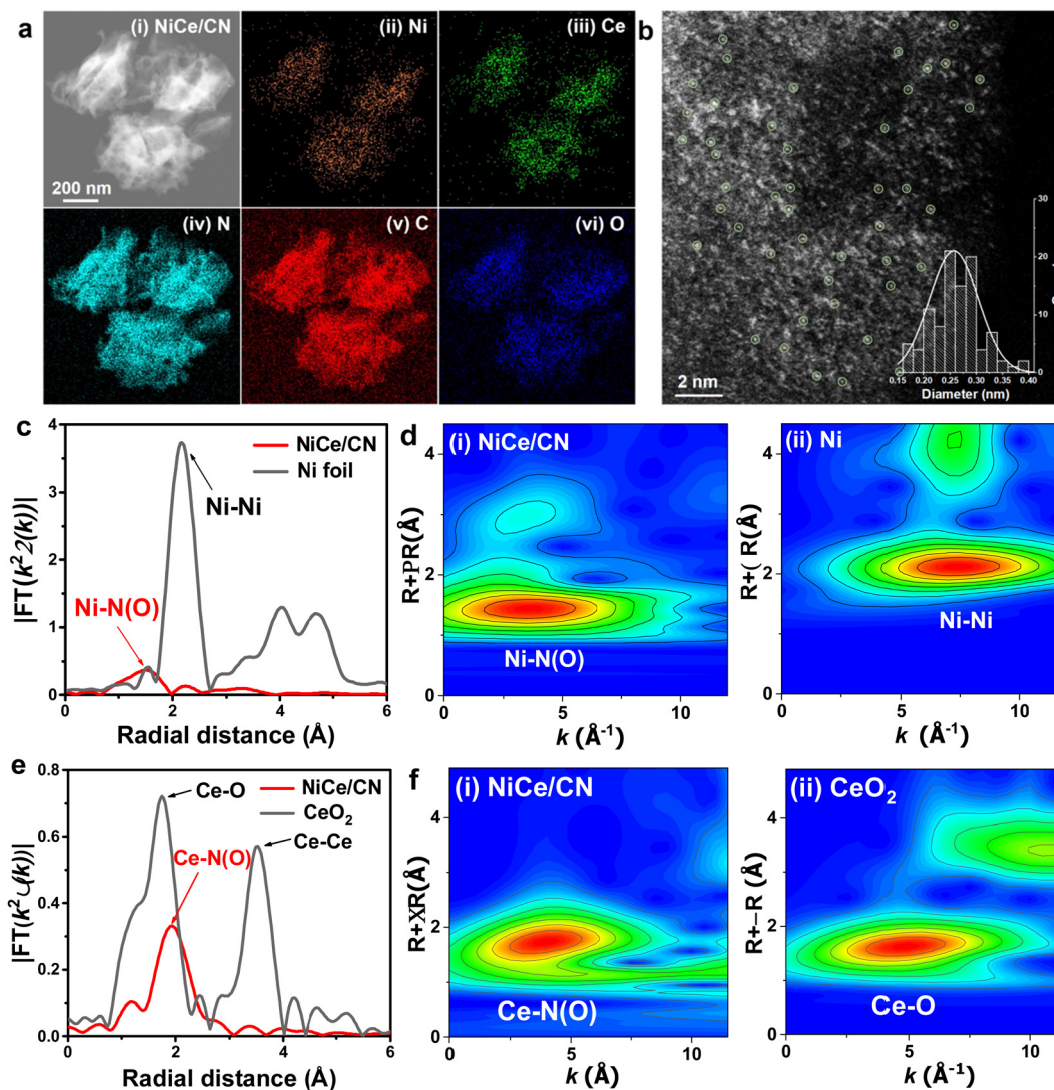


**Fig. 1** Characterizations of the fresh NiCe/CN DAC. (a, i) TEM image, (a, ii-vi) elemental mappings and (b) AC HAADF-STEM image of NiCe/CN DAC-fresh; (c) FT-EXAFS spectra and (d) wavelet transform analysis for the Ni K-edge of (i) NiCe/CN DAC and (ii) Ni foil; (e) FT-EXAFS spectra and (f) wavelet transform analysis for the Ce K-edge of (i) NiCe/CN DAC and (ii) CeO$_2$.

reveal the valence states and the coordination environments of the metal atom centers, in which the Fourier-transformed extended X-ray absorption fine structure (FT-EXAFS) analysis and wavelet transform (WT) analysis provide an intuitive way of further ascertaining the dispersion state of metal atoms in the NiCe/CN DAC through the comparison with reference samples. As shown in Fig. 1c, the Fourier transformed $k^3$-weighted $\chi(k)$-function of the EXAFS spectrum for NiCe/CN DAC shows only one characteristic peak at around 1.49 Å. This peak can be assigned to the Ni–N(O) scattering of the atomic Ni coordinated with N(O), which distinguishes from the peak corresponding to metallic Ni–Ni scattering at ~2.16 Å in Ni foil.[32] The WT of the EXAFS spectrum for the Ni K-edge of NiCe/CN DAC shows the characteristic peak of the Ni–N(O) bond at 3.35 Å that can be assigned to the atomic Ni–N(O) species (Fig. 1d(i)). The WT of the EXAFS spectrum for the Ni K-edge of Ni foil shows the Ni–Ni bond at 7.4 Å$^{-1}$ that can be attributed to Ni particles (Fig. 1d(ii)). Meanwhile, two distinct peaks appear at 1.75 Å and 3.52 Å in the EXAFS spectrum of the Ce K-edge of the CeO$_2$ sample (Fig. 1e). The former is due to the Ce–O scattering and the latter is attributed to the Ce–Ce scattering, respectively. NiCe/CN DAC shows only one peak derived from Ce–N(O) scattering at about 1.93 Å. As shown in Fig. 1f(i), the WT of the EXAFS spectrum on the Ce K-edge of NiCe/CN DAC shows the characteristic peak of the Ce–N(O) bond at 3.93 Å$^{-1}$, while CeO$_2$ shows the characteristic peak of the Ce–O bond at 4.73 Å$^{-1}$ (Fig. 1f(ii)), which further confirms the co-existence of isolated Ni and Ce sites, consistent with the above HADDF-STEM results. According to the EXAFS fitting parameters in Table S1 (ESI†), each isolated Ni and Ce atom is coordinated by N atoms and (or) O atoms (note that it is difficult to discern N and O coordinates by EXAFS fitting due to their similar atomic numbers).[54] The Ni–N(O) shows a coordination number of 5.8 at a distance of 2.04 Å, while Ce–N(O) shows a higher coordination number of 12.1 at a distance of 2.59 Å. Considering the strong affinity with the oxygen of Ce, it is easy to absorb O$_2$ from the atmosphere and then form the structure with high coordination number.[55] Combined with the detailed information of the metal loadings determined by inductively coupled plasma atomic emission spectroscopy (ICP-AES, Table S2, ESI†), atomically dispersed NiCe/CN DAC could be obtained even though the metal loadings increased to 2.2 wt% and 4.9 wt% for Ni and Ce elements, respectively. The TEM characterizations were also performed on the sample of the spent NiCe/CN DAC, in which the image (Fig. S4a, ESI†) shows that the atoms were slightly agglomerated after the reaction. The elemental mappings (Fig. S4d, ESI†) indicate that the metal dispersion was still relatively homogeneous with a considerable amount of metal present as atoms or clusters, in addition to the formation of nanoparticles. Quantitative analysis of the mass loss of spent NiCe/CN DAC was performed using thermogravimetry analysis (TGA, Fig. S5, ESI†). During the detection under flowing N$_2$, the mass loss of spent NiCe/CN DAC was ~10% at the highest reaction temperature of 623 K, which suggests that there might be a small amount of CN support decomposition during catalysis.

## Catalytic performance in methanol steam reforming and water–gas shift reaction over NiCe/CN DAC

In general, the MSR reaction (eqn (S8), ESI†) consists of MD (eqn (S9), ESI†) and WGS (eqn (S10), ESI†). The activity of WGS affects not only the generation rate of H$_2$, but also the content of CO in the steam, which will reduce the efficiency of direct methanol fuel cells (DMFCs) as consequential applications.[4] Therefore, we tested the catalytic performance of NiCe/CN DAC in MSR and WGS, respectively. Clearly, complete methanol (for MSR) or CO (for WGS) conversion would be determined at elevated temperatures over various amounts of NiCe/CN DAC (Fig. S6, ESI†). The Ni–Ce bi-atomic center was found to facilitate both MSR and WGS reactions. With the increase of the catalyst content, the reactivity increased. In particular, the activity of WGS increased significantly. For instance, the CO conversion of 20 mg catalyst was only 2.5%, which increased to 21.4% over 50 mg catalyst, and even to 94.1% over 100 mg catalyst at 533 K (Fig. S6b, ESI†).

Then, the catalytic performances of a few Ni-based reference samples have been evaluated containing multiple rare-earth elementals, such as La and Y-decorated Ni-DACs, as well as Ni/CN single atom catalyst (SAC) and Ce/CN SAC in the MSR. As shown in Fig. 2a, compared with other catalysts, NiCe/CN DAC exhibited the highest activity below 513 K, at which methanol firstly approached complete conversion, and Fig. 2b shows the superior hydrogen evolution rate of NiCe/CN DAC than other catalysts. Ce is a better back-bone component within the Ni-based DACs compared with La and Y, which show slight promotion or inhibition against Ni/CN SAC on MSR. All of these samples are more active than Ce/CN SAC (Fig. 2a and b), which shows negligible activity during catalysis. In addition, the Ni/CeO$_2$ possesses significant amounts of Ni–CeO$_x$ pairs and showed pretty good activity in MSR (Fig. 2a and b). The modified NiCe/CN DAC showed better activity than the Ni/CeO$_2$ and Pt/Al$_2$O$_3$ catalyst (Fig. 2a and b). Also, the apparent activation energies for the abovementioned catalysts were calculated following Arrhenius plots (Fig. S7a and Table S3, ESI†). The order of the apparent activation energies among these catalysts compared on MSR is basically consistent with that of the activities, wherein NiCe/CN DAC shows the lowest apparent reaction barrier of 63.5 kJ mol$^{-1}$. This confirms that NiCe/CN DAC has excellent catalytic performance on MSR.

NiCe/CN DAC is more active than Pt/Al$_2$O$_3$ or any other noble metal catalysts, such as the Pd-based and Ru-based catalysts listed in Table S4 (ESI†). In addition, compared with other Ni-based catalysts, NiCe/CN DAC achieved complete methanol conversion at relatively low temperature, except the conversion determined on 7% Cu–3% Ni/Al$_2$O$_3$ catalyst (~94% at 498 K), in which 3 g catalyst was applied to the reaction (Table S4, ESI†). It is probable that the Ni–CeO$_x$ DACs containing dual atomically dispersed active sites could help people solve the abovementioned problems.

The selectivity of CO and the hydrogen generation rate would be affected by the activity of WGS. Therefore, the catalyst should have significant reactivity on WGS under relatively mild conditions. From Fig. S8 (ESI†), NiCe/CN DAC had low CO
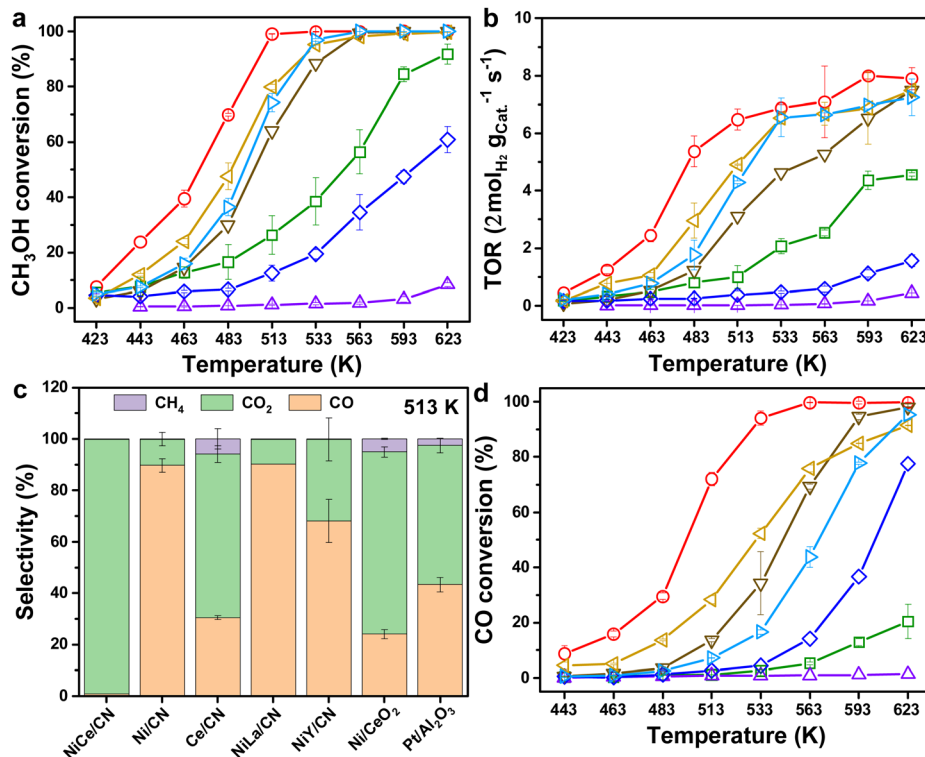
**Fig. 2** Catalytic performances of NiCe/CN DAC in MSR and WGS. (a) $CH_3OH$ conversion, (b) TOR of $H_2$ generation, (c) the comparison of carbon product selectivities of NiCe/CN DAC and reference samples at 513 K in MSR; (Reaction conditions: 1 kPa $CH_3OH$, 16.02 kPa $H_2O$, Ar balanced, GHSV = 318 $h^{-1}$) (d) CO conversion of NiCe/CN DAC and reference samples in WGS. (Reaction conditions: 2 kPa CO, 10 kPa $H_2O$, Ar balanced, GHSV = 848 $h^{-1}$, red ○: NiCe/CN DAC, brown ▽: NiLa/CN DAC, sapphire ◇: NiY/CN DAC, green □: Ni/CN SAC, purple △: Ce/CN SAC, yellow ◁: Ni/CeO₂, blue ▷: Pt/Al₂O₃.)

selectivity across the overall temperature range (423–623 K), with a maximum of 16.0% at 463 K. When the temperature increased to 513 K, the CO selectivity dropped to 0.8% with the methanol conversion at 99.1%. In addition to the highest $CH_3OH$ conversion, NiCe/CN DAC showed the lowest CO selectivity at 513 K (Fig. 2c). As for the $Ni/CeO_2$ and $Pt/Al_2O_3$ catalysts prepared by the impregnation method, the CO selectivities were constantly high at 24.0% and 43.3% at 79.9% and 74.3% $CH_3OH$ conversion, respectively. Both showed significant $CH_4$ selectivity following the side reaction of carbon dioxide methanation. The CO selectivities of other Ni-based monatomic and diatomic catalysts were also relatively high, indicating that the activity of WGS on NiCe/CN DAC is much greater than that of the other catalysts compared under the same reaction conditions.

As shown in Fig. 2d, the activities of NiCe/CN DAC on WGS were the best within the samples compared, resulting in low CO selectivity (Fig. 2c) and significant hydrogen generation (Fig. 2b). Additionally, Ce/CN SAC showed almost no activity on WGS (conversion was 1.3% at 623 K), which might be attributed to the absence of Ni-sites for CO activation. Simultaneously, NiLa/CN DAC showed greater activities of MSR and WGS than Ni/CN SAC, indicating the positive promoting effect of the Ni–La diatomic structure. Notably, the activity of MSR on NiY/CN DAC was worse than that of Ni/CN SAC, while the activity of WGS was better. We suggest that the introduction of

Y may increase $O_V$ to some extent, which is conducive to the activation of $H_2O$, while the amount of $O_V$ was far less than that brought by the introduction of Ce. The decoration of Y might not preserve the active site of Ce for this whole reforming reaction, or the potential interaction between Ni and Y may inhibit the activation of $CH_3OH$. As shown in Fig. S7b and Table S3 (ESI†), the apparent activation energies for the above catalysts were estimated following Arrhenius plots, where NiCe/CN DAC shows the lowest apparent reaction barrier of 60.5 kJ $mol^{-1}$, corresponding to its best catalytic performance of WGS. The activation energy values of WGS over NiLa/CN DAC, $Ni/CeO_2$ and $Pt/Al_2O_3$ were similar, since the activities of WGS over them were also similar. The activity of NiY/CN DAC was worse than that of NiCe/CN DAC and NiLa/CN DAC. The activation energy (77.1 kJ $mol^{-1}$) was significantly higher than that of the latter two dual-atomic catalysts (65.4 kJ $mol^{-1}$ for NiLa/CN DAC), indicating that the ability of the Ce center to activate $H_2O$ is greater than that of the La and Y centers in the dual-atomic structure. Compared with the diatomic catalysts, the values of activation energy of Ni/CN SAC and Ce/CN SAC were 79.7 kJ $mol^{-1}$ and 194.2 kJ $mol^{-1}$, respectively. We hypothesized that the existence of the Ni site or the Ce site alone was not conducive to the activation of $H_2O$ and CO. The dual active site Ni–$CeO_x$ could activate CO and $H_2O$ simultaneously, which was the key to the excellent activity of WGS. Furthermore, the NiCe/CN DAC stability test on MSR was

performed at 623 K. The result shows that the activity was unchanged within 10 hours (Fig. S9, ESI†). Based on these results, it is reasonable to deduce that the special interface between Ni and Ce is important and might be responsible for the excellent catalytic performance of NiCe/CN DAC on MSR and WGS.

To further determine the active species of NiCe/CN DAC during MSR, quasi-*in situ* XPS analysis was selectively applied. For the NiCe/CN DAC sample, the spectrum of Ni $2p_{3/2}$ can be deconvoluted into two species at 854.4 and 856.7 eV under MSR condition (Fig. 3a(iii)), which can be attributed to the oxidized $Ni^{2+}$ and $Ni^{3+}$ species, respectively.[56] In contrast, for the Ni/CN SAC, the peak positions of the Ni $2p_{3/2}$ species are located at 855.4 and 857.7 eV (Fig. S10(iii) and Table S5, ESI†). Compared with the Ni/CN SAC, the binding energy of the Ni species in NiCe/CN DAC was negatively shifted by approximately 1 eV, indicating a more electron-rich feature of the Ni atoms in NiCe/CN DAC than Ni/CN SAC as the electron transfer from Ce to Ni. For Ni/CN SAC and NiCe/CN DAC, after the reduction of $H_2$ (Fig. S10(i) and Fig. 3a(i), ESI†), only the oxidized Ni species ($Ni^{2+}$ and $Ni^{3+}$) could be observed, and no metallic Ni ($Ni^0$) appeared.[32,57] After introducing methanol for 1 h (Fig. S10(ii) and Fig. 3a(ii), ESI†), the binding energy of the Ni species was slightly negatively shifted, and a small portion of metallic Ni appeared. This is probably due to a slight agglomeration of Ni atoms to generate small clusters, or owing to the gaining of electrons. Meanwhile, the XPS spectra of Ce 3d have also been measured to further investigate the amount of $Ce^{3+}$ and the

changes in the valence state of Ce under the same treatment (Fig. 3b and Table S6, ESI†).[57,58] Similar to that observed for the Ni species, the content of $Ce^{3+}$ increased and the average valence state decreased significantly after the introduction of methanol in NiCe/CN DAC (Fig. 3b(ii)). This did not change when the mixture of methanol and water vapor was continuously fed (Fig. 3b(iii)). The change in the valence state of Ce in Ni/CeO₂ (Fig. S11b, ESI†) was similar to that in NiCe/CN DAC. Nevertheless, the variation of the Ni (Fig. S11a, ESI†) was opposite of that in NiCe/CN DAC, with a slight increase, suggesting that a small number of electrons transfer from Ni to Ce during the reaction or due to slight oxidation during MSR by water. This may also account for the difference in activity between the two catalysts.

### Reaction mechanism of MSR on NiCe/CN DAC

**Steady-state isotopic transient kinetic analysis (SSITKA) combined with *in situ* FTIR Measurements over NiCe/CN DAC.** The SSITKA-FTIR technique has shown to be very useful in obtaining details on the adsorption and desorption of intermediates that could be involved in the reaction of MSR. Therefore, isotope exchange experiments of $CH_3OH$ and $CD_3OD$ were applied to clarify the adsorption/desorption of methoxy groups (Fig. 4a). The infrared spectrum was recorded after the adsorption of $CH_3OH$ reached saturation as the background, and then switched to $CD_3OD$ until another adsorption saturation reached. The positive peaks in Fig. 4a represent the adsorption of the labeled reactant and the inverted peaks
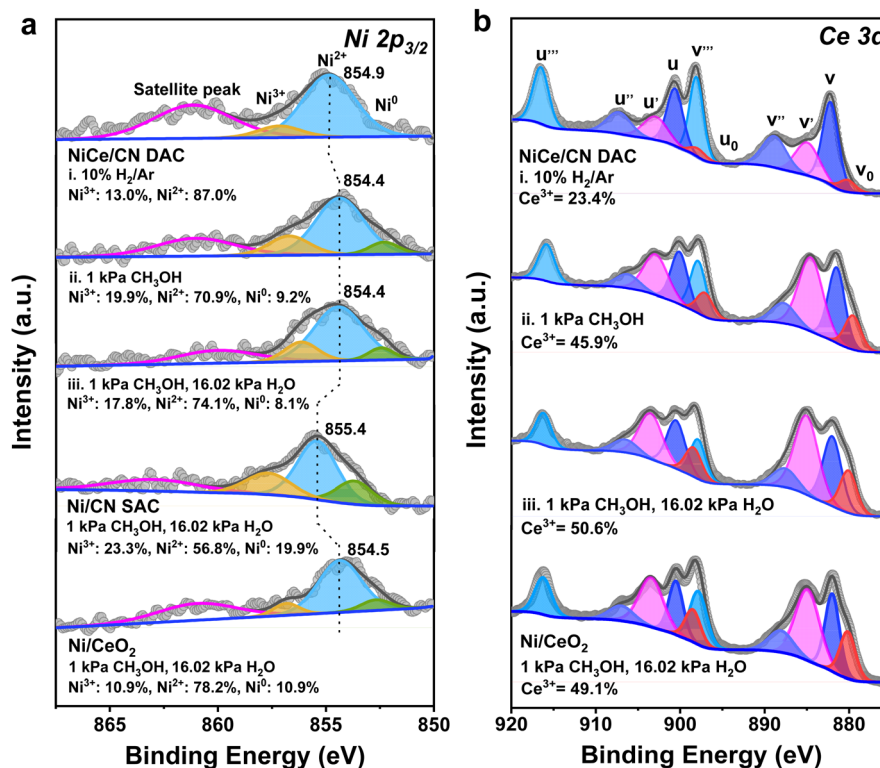


**Fig. 3** Quasi-*in situ* XPS characterization of the NiCe/CN DAC and reference samples under different reaction conditions. (a) Ni 2p and (b) Ce 3d XPS spectra after reduction (i: 10% H₂/Ar, 623 K, 2 h, 50 mL min⁻¹), after introduction of CH₃OH for 1 h (ii: 1 kPa CH₃OH, Ar balanced, 623 K, 30 mL min⁻¹) and under MSR condition for 1 h (iii: 1 kPa CH₃OH, 16.02 kPa H₂O, Ar balanced, 30 mL min⁻¹).

represent the desorption of the unlabeled reactant. The characteristic features of the methoxy, formate, formyl and hydroxyl functional groups were identified as described in Fig. 4a, in which the bands at 3100 cm$^{-1}$, ~3600 cm$^{-1}$ and 2320 cm$^{-1}$, ~2600 cm$^{-1}$ were assigned to the stretching vibration of the O–H bond ($\nu_{OH}$) in hydroxyl groups[59] and the O–D bond ($\nu_{OD}$) in DO* groups,[60] respectively. The feature at 2980 cm$^{-1}$ was assigned to the asymmetric vibration of the C–H bond ($\nu_{as,CH}$) in gaseous methanol.[59] The features at 2929 and 2820 cm$^{-1}$ were assigned to the asymmetric vibration of the C–H bond ($\nu_{as,CH}$), and symmetric vibration of the C–H bond ($\nu_{s,CH}$) of the methoxy species (CH$_3$O*),[59] respectively, and 2894 cm$^{-1}$ was assigned to the stretching vibration of the C–H bond ($\nu_{CH}$) of the formate species (HCOO*).[57,59] The band at 2710–2720 cm$^{-1}$ was associated with the stretching vibration of the C–H bond ($\nu_{CH}$) of the adsorbed formyl group (HCO*).[61] The band at 2000 cm$^{-1}$, ~2300 cm$^{-1}$ was attributed to the vibration of C–D bond in CD$_3$O* or DCOO*, in which the features at 2250 and 2100 cm$^{-1}$ were the analog to the band of $\nu_{as,CH}$ of CH$_3$O* at 2929 cm$^{-1}$ and $\nu_{CH}$ of HCOO* at 2894 cm$^{-1}$, respectively.[60–62] The feature at 1700 cm$^{-1}$ was related to the stretching vibration of the C=O bond ($\nu_{C=O}$) of HCO*.[61] The peak at 1573 cm$^{-1}$ was assigned to the asymmetric vibration of the O–C–O bond ($\nu_{as,OCO}$) in HCOO*,[57,59] and the isotope-shifted analog at 1351 cm$^{-1}$ was assigned to the vibration of the O–C–O bond in DCOO*.[62] The peak at 1440 cm$^{-1}$ was assigned to the asymmetric bending vibration of the C–H bond ($\delta_{as,CH}$) in HCOO*.[36,62] The band at 1000 cm$^{-1}$, ~1080 cm$^{-1}$ was assigned to the stretching vibration of the C–O bond ($\nu_{CO}$) in CH$_3$O*.[59] At last, the features at 1115 and 1130 cm$^{-1}$ were attributed to the bending vibration of the CD$_2$ bond ($\delta_{CD_2}$) of the CD$_3$O* and the resonance of the symmetric bending vibration of CD$_3$ bond ($\delta_{s,CD_3}$) band with the $\nu_{CO}$ mode in CD$_3$O*.[60] The peak fitting diagram of the infrared spectrum after the saturated adsorption of CD$_3$OD (ca. ~50 min) is shown in Fig. S12 (ESI†). The

trend of the normalized area of the methoxy peak over time is given (Fig. 4b). The fitted result suggests that methoxy groups may adsorb on a single site (single pool from the fittings, eqn (12), Table 1).[63] Similarly, the adsorption/desorption of water (or hydroxyl groups) was clarified through the isotope exchange experiments of D$_2$O and H$_2$O (Fig. S13, ESI†). The fitted result suggests that water (or hydroxyl groups) may also adsorb on only one site, and the adsorption strength of methoxy groups is much greater than that of water derivatives (Fig. 4b and Table 1). To further distinguish the adsorption sites of the methoxy and hydroxyl species, the isotope exchange experiments of CH$_3$OH and CD$_3$OD with different pressures of H$_2$O co-fed were carried out (Fig. S14 and S15, ESI†). As shown in Fig. 4b and Table 1, the residual coverage ($\Theta_{des}$) of the methoxy groups remained unchanged, suggesting that the presence of water does not affect the adsorption and desorption of methanol. Furthermore, the absence of competitive adsorption between the hydroxyl and methoxy groups supports that they adsorb on independent sites. Based on these results, it is reasonable to deduce that water (or hydroxyl) may adsorb on CeO$_x$ sites of the NiCe/CN DAC, and methoxy groups were mainly adsorbed on the Ni sites of the NiCe/CN DAC (at least the dehydrogenation of CH$_3$O- happens at the Ni sites). If the dissociative adsorption of methanol and the activation of water mainly occur on the Ni and CeO$_x$ sites, respectively, then the interface between them would be very important to connect MD and WGS and facilitate the whole MSR reaction.

**Pressure dependence study of the MSR reaction over NiCe/CN DAC.** To clarify the reaction mechanism of MSR on NiCe/CN DAC, a systematic kinetic study has been applied. As shown in Fig. S16 (ESI†), the conversion of CH$_3$OH was plotted as a function of the reciprocal of the gas hourly space velocity (GHSV$^{-1}$). The external mass/heat transfer limitation would be selectively excluded in the range of linear correlation with an intercept of zero, and the Koros–Nowak criterion was applied to
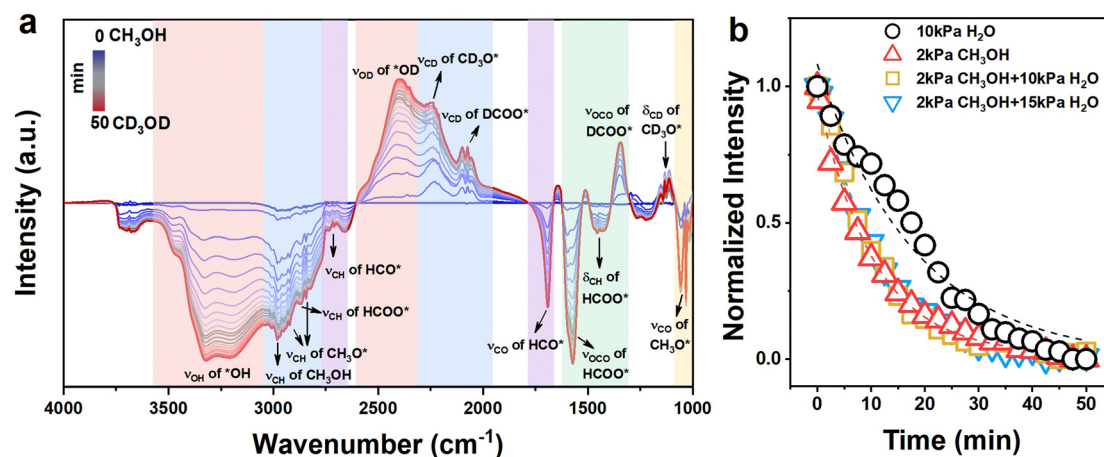


**Fig. 4** SSITKA combined with *in situ* FTIR measurements on NiCe/CN DAC. (a) IR spectra of NiCe/CN DAC recorded at 623 K during a SSITKA experiment from the initial flow made of 2 kPa CH$_3$OH in Ar to a similar labeled (2 kPa CD$_3$OD) gas-mixture (total flow rate: 50 mL min$^{-1}$). (b) The normalized intensities of surface species in CH$_3$OH-CD$_3$OD, H$_2$O–D$_2$O and CH$_3$OH + H$_2$O-CD$_3$OD + H$_2$O with various pressures of H$_2$O exchange experiments on NiCe/CN DAC as a function of time (black ○: desorption of DO-; red △: desorption of CH$_3$O-; yellow □: desorption of CH$_3$O- with 10 kPa H$_2$O co-feed; blue ▽: desorption of CH$_3$O- with 15 kPa H$_2$O co-feed). Dotted lines are fitted curves.

**Table 1** Expressions of the desorption rate and corresponding models for different species fitted by desorption branch curves in Fig. 4(b)

| Species | $\Theta_{des}$ | $\tau = \dfrac{1}{k}$ |
|---|---|---|
| ○-OH | $\Theta_{des} = 19.56 \times 0.55 \times e^{-0.55 \times t}$ | 17.9 |
| △-CH$_3$O | $\Theta_{des} = 1.12 \times 0.85 \times e^{-0.85 \times t}$ | 10.6 |
| □-CH$_3$O | $\Theta_{des} = 1.11 \times 0.93 \times e^{-0.93 \times t}$ | 11.1 |
| ▽-CH$_3$O | $\Theta_{des} = 1.09 \times 0.96 \times e^{-0.96 \times t}$ | 11.2 |

eliminate the internal diffusion limitations.[64] All pressure dependency experiments were carried out at the CH$_3$OH conversion <5% to ensure that the reaction runs under the differential conditions. The dependencies of the CH$_3$OH, H$_2$O, CO and CO$_2$ pressures on the H$_2$ formation rates ($r_{H_2}$) and H$_2$ pressure on the CH$_3$OH consumption rate ($r_{CH_3OH}$) have been determined at various reaction temperatures (*i.e.*, 513 K; 573 K; 623 K). As described in Fig. 5a, the H$_2$ formation rates decreased with CO pressure at all three temperatures. As the coverage of CO decreased, the dependencies of H$_2$ formation on the CO pressure rose with the temperature increasing (513 K: $r_{H_2} \sim [CO]^{-0.9}$; 573 K: $r_{H_2} \sim [CO]^{-0.3 \text{ to } -0.7}$; 623 K: $r_{H_2} \sim [CO]^{-0.4}$), which suggests that CO is significant on the surface of the catalyst and inhibits hydrogen production. The H$_2$ formation rates increased with CH$_3$OH pressure below 3 kPa, and then decreased at 513 K and 573 K or remained essentially constant at 623 K with the CH$_3$OH pressure increasing, respectively (513 K: $r_{H_2} \sim [CH_3OH]^{0.6 \text{ to } -0.6}$; 573 K: $r_{H_2} \sim [CH_3OH]^{0.3 \text{ to } -0.3}$; 623 K: $r_{H_2} \sim [CH_3OH]^{0.9-0.1}$. Fig. 5b). The initial nearly first-order dependence indicates that active sites are not saturated with CH$_3$OH or its derivatives (CH$_3$O*). The later negative dependence at 513 K and 573 K suggest that more CH$_3$OH was present with a high coverage once methanol was continuously introduced, possibly owing to the increase of CO

generated by continuous dehydrogenation of CH$_3$OH. The CO generated continuously was difficult to desorb and accumulated on the surface of the catalyst with a little carbon deposition, suppressing the hydrogen formation. This inhibition diminished as the temperature increased since the coverage of surface species decreased and the surface species became more susceptible to desorption, showing a zero-order dependence of H$_2$ formation rate over CH$_3$OH pressure at 623 K. It also suggests that CH$_3$OH and its derivatives (CH$_3$O*) may be one of the most abundant surface intermediates (MASIs) over the catalyst. The more negative order dependencies on CO pressure suggests that CO is also significant from the catalytic surface.

Simultaneously, the H$_2$ formation rates were almost independent of H$_2$O pressure with nearly zero-order dependencies at all three temperatures (513 K: $r_{H_2} \sim [H_2O]^{-0.1}$; 573 K: $r_{H_2} \sim [H_2O]^{0}$; 623 K: $r_{H_2} \sim [H_2O]^{0.1}$. Fig. 5c). This suggests that either H$_2$O (or its derivatives: –OH) is abundant on the surface of the catalyst, or WGS is not significant during catalysis under this differential reaction condition. We have two methods to determine the contribution of WGS within the whole reaction network, one of which is to compare the selectivities of the carbonaceous species. For example, if the main product is CO$_2$ rather than CO, WGS must be significant within the whole reaction process. If CO is the main species, the reaction would experience limited WGS. The other method is to check the ratio between H$_2$ and CO ($\varepsilon = f_{H_2}/f_{CO}$) within the downstream gases to decide the rate ratio between MD and WGS ($\eta = r_{MD}/r_{WGS}$), which was systematically discussed in Section 6 of the ESI† (ESI-S6). There was still a fair amount of CO during the kinetic measurement at low H$_2$O pressure (<15 kPa, Fig. S17b, ESI†), which suggests that WGS is not probably significant under the reaction conditions in Fig. 5c. Therefore, under these
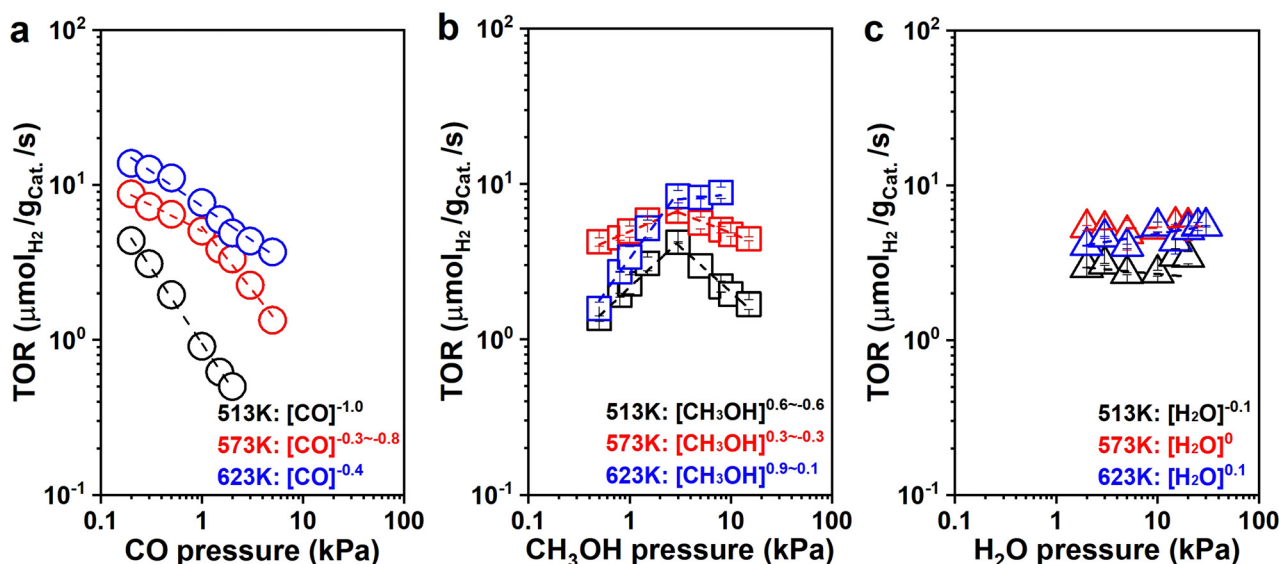


**Fig. 5** Pressure dependence study of MSR on NiCe/CN DAC. H$_2$ formation rates as functions of the (a) CO pressures (○: 0.2−3 kPa CO, 1 kPa CH$_3$OH, 16.02 kPa H$_2$O), (b) CH$_3$OH (□: 0.5−8 kPa CH$_3$OH, 16.02 kPa H$_2$O), and (c) H$_2$O (△: 2−30 kPa H$_2$O, 1 kPa CH$_3$OH) of MSR reaction at different temperatures and atmospheric pressure.

conditions, we found that WGS has weak contributions to the formation of $H_2$ during MSR with the $H_2O$ pressure increasing from 2 kPa to 15 kPa. The $\varepsilon$ decreased from 8.9 to 1.6 (Fig. S17a, ESI†), which is consistent with the results learned from SSITKA. It is probable that WGS becomes significant once the total conversion is selectively promoted, which is quite similar to the condition reported in the literature.[10,12] For example, as described in Fig. S18a (ESI†), ratios on the reaction rate of MD and WGS ($\varepsilon$) decreased from 1.2 to 1.0 once the reaction conversion was promoted from 7.7% to 99.1%, respectively.

As shown in Fig. S19a (ESI†), the $H_2$ formation rates were also independent of the $CO_2$ pressure with zero-order dependence at all three temperatures (513 K: $r_{H_2} \sim [CO_2]^{-0.1}$; 573 K: $r_{H_2} \sim [CO_2]^{0}$; 623 K: $r_{H_2} \sim [CO_2]^{0}$). Moreover, the $CH_3OH$ consumption rates were independent of $H_2$ pressure with nearly zero-order dependence at all three conditions (513 K: $r_{CH_3OH} \sim [H_2]^{0}$; 573 K: $r_{CH_3OH} \sim [H_2]^{-0.1}$; 623 K: $r_{CH_3OH} \sim [H_2]^{0}$, Fig. S19b, ESI†), suggesting that although $CO_2$ and $H_2$ are significant in the reaction system, the binding energy of $CO_2$ and $H_2$ or its derivatives (*i.e.*, H*) is weaker than the MASIs promoted. It is worth noting that large amounts of $H_2$ slightly inhibited the reaction activity, and it becomes more pronounced at lower temperatures.

To explore the intermediates on the catalyst surface under the condition of WGS and develop a deeper understanding of the reaction mechanism of MSR, pressure dependence studies for WGS were conducted. As shown in Fig. S20 (ESI†), the $H_2$ formation rate increased with CO pressure below 0.8 kPa and then maintained essentially constant at 573 K with the CO pressure promoted, respectively ($r_{H_2} \sim [CO]^{0.4-0}$). The initial positive dependence indicates that active sites are not saturated with CO, and the later zero-order dependence indicates that the CO* would be significant at high CO partial pressures. The $H_2$ formation rate was independent of $CO_2$ pressure with zero-order dependence ($r_{H_2} \sim [CO_2]^{0}$), suggesting that the $CO_2$ is either negligible or significant on the surface of the catalyst. As the adsorption of $CO_2$ is difficult from highly dispersed transition metals, we would suggest that the coverage of $CO_2$ from the catalytic surface is negligible.[65–67] The $H_2$ formation rates increased with $H_2O$ pressure with the nearly first-order dependence ($r_{H_2} \sim [H_2O]^{0.6}$), then $H_2O$ or –OH may not be the MASIs on the surface of catalysts. The $CO_2$ formation rates decreased with $H_2$ pressure with the nearly negative first-order dependence ($r_{CO_2} \sim [H_2]^{-0.8}$), indicating that $H_2$ or its derivatives (*i.e.*, H*) may be significant on the surface of catalysts for the WGS reaction. This is slightly different from our previous $Pt/NiAl_2O_4$ reaction system detected.[28]

With all of the information received, a possible reaction pathway has been proposed, as shown in Scheme 1. We assume that the activation of $CH_3OH$ and $H_2O$ occurred at different active sites, with Ni and $CeO_x$ acting as the primary active sites for MD and WGS, respectively, resulting in the interface between Ni and $CeO_x$ as the critical active components of

**Methanol Dehydrogenation**



**Water-Gas Shift Reaction**
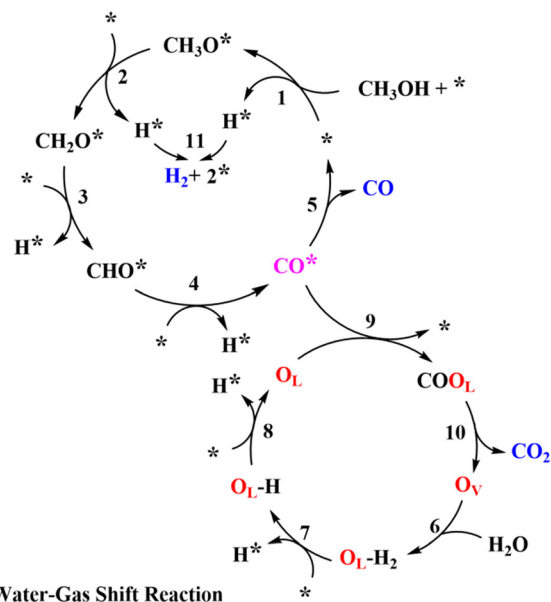
Scheme 1    Proposed reaction pathway of MSR over NiCe/CN DAC.

MSR. In Scheme 1, first, $CH_3OH$ dissociatively adsorbed to form methoxy groups ($CH_3O^*$) and protons (H*, * represents the Ni site). The methoxy groups on the Ni sites further dehydrogenate to $CH_2O^*$ and H*, and $CH_2O^*$ would undergo additional dehydrogenation steps to selectively generate CO. All protons would adsorb (or diffuse) to the Ni sites to form H*, the two of which would combine to create a molecularly adsorbed hydrogen and release one active site (*). Finally, the desorption of hydrogen would release another active site. In addition, we assume that $H_2O$ was activated at the oxygen vacancy ($O_V$) of $CeO_x$ to form $O_LH$ groups and H*, which would further dehydrogenate to form $O_L$ and H*. The CO adsorbed on the Ni sites ($CO^*$) would transfer to $O_L$ sites to form the $COO_L$ species, eventually releasing $CO_2$ and regenerating the oxygen vacancies ($O_V$). The H* would spontaneously diffuse to the Ni sites and release as $H_2$.

The detailed elementary steps are presented in Scheme S1 (ESI†), and the complete derivations of the rate expression for $H_2$ formation in MD and WGS are listed in Section 7 of the ESI† (ESI-S7). It was hypothesized that the formation of $CH_2O^*$ from the $CH_3O^*$ dehydrogenation may be the kinetically relevant step (KRS) for MD, and the cracking of $O_LH$ may be the KRS for WGS:

$$CH_3O^* + * \rightarrow CH_2O^* + H^* \tag{1}$$

$$O_LH + * \rightarrow H^* + O_L \tag{2}$$
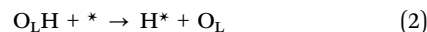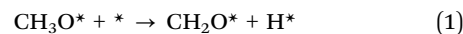
According to the assumption that MSR undergoes both MD and WGS processes, the expression of the $H_2$ formation rates in MSR would be expressed as follows:

$$r_{H_2} = r_{MD} + r_{WGS}\frac{r}{[L]} = \frac{k_2 K_1 K_{11}^{\frac{1}{2}}[CH_3OH] + k_8 K_6 K_7 K_{11}^{\frac{1}{2}}[H_2O]}{[H_2]^{\frac{1}{2}}\left(1 + \frac{[H_2]^{\frac{1}{2}}}{K_{11}^{\frac{1}{2}}} + \frac{[CO]}{K_5} + \frac{K_1 K_{11}^{\frac{1}{2}}[CH_3OH]}{[H_2]^{\frac{1}{2}}}\right)\left(1 + \frac{[CO_2]}{K_{10}} + \frac{K_6 K_7 K_{11}^{\frac{1}{2}}[H_2O]}{[H_2]^{\frac{1}{2}}}\right)} \tag{3}$$

**Table 2** Calculated KIEs for MD, WGS and MSR

| Isotope tracing | MSR | MD | WGS |
|---|---|---|---|
| $D_2O \rightarrow H_2O$ | 1.35 | — | 2.56 |
| $CD_3OD \rightarrow CH_3OH$ | 1.72 | 1.81 | — |
| $CH_3OD \rightarrow CH_3OH$ | 1.12 | 1.19 | — |

By assuming different surface species as the main surface intermediates, the expression (eqn (3)) could meet the pressure dependence results (Fig. 5 and Fig. S19, ESI†) very well. Thus, this MSR reaction might experience two parallel paths that contain MD and WGS, in which the rupture of C–H bond within $CH_3O^*$ and the cracking of $O_LH$ are the KRSs, respectively.

**Isotope tracing and kinetic isotope effects assessment over the NiCe/CN DAC.** To confirm the KRS proposed, isotope tracing and kinetic isotope effects assessment during MD, WGS and MSR were systematically investigated (Table 2 and ESI-S9, ESI†), in which ordinary reagents were replaced by isotopic reactants and back to normal molecules stepwise to estimate the deactivation and kinetic isotope effects (KIEs). As for the MD shown in Fig. S21 (ESI†), when $CD_3OD$ was replaced by $CH_3OD$, the KIE estimated on the change of $H_2$ formation rates was 1.81 ($k_H/k_D \sim 1.81$, Table 2), which confirms the normal primary isotopic effects.[68] In addition, compared with the KIE obtained from $CH_3OD$ replaced by $CH_3OH$ ($k_H/k_D \sim 1.19$, Table 2), this obvious KIE is consistent with the cracking of the C–H bond in $CH_3OH$ is the KRS. As for WGS shown in Fig. S22 (ESI†), an obvious KIE ($k_H/k_D \sim 2.56$, Table 2) could be obtained when $D_2O$ was replaced by $H_2O$, indicating the cracking of O–H should be involved in the KRS of the WGS reaction. Meanwhile, in MSR (Fig. S23, ESI†), when $CD_3OD$ was replaced by $CH_3OD$ and then by $CH_3OH$, KIEs similar to that in MD were obtained simultaneously ($k_H/k_D \sim 1.72$, $k_H/k_D \sim 1.12$, Table 2). This indicated that the cracking of the C–H bond in $CH_3OH$ may still be the KRS in MSR. Meanwhile, the KIE of $D_2O$ replaced by $H_2O$ was 1.35 ($k_H/k_D \sim 1.35$, Table 2) during the MSR reaction, which is smaller than that in the bare WGS test, suggesting a normal secondary isotopic effect.[67] This is also in good agreement with the assumption that the contribution of WGS to hydrogen formation under this differential reaction condition (ca. 1 kPa $CH_3OH$, 2 kPa $H_2O$, Ar balanced, 623 K, GHSV = 19 099 $h^{-1}$) is negligible.

Similar to the rate expression of $H_2$ formation in MSR (eqn (3)), the KIEs of MSR may also be described as the synergistic effect of the MD and WGS reactions:

$$KIE_{MSR} = \alpha \cdot KIE_{MD} + \beta \cdot KIE_{WGS} \qquad (4)$$

where $\alpha$ and $\beta$ are all constants.

## Conclusions

A dual-atomic catalytic system has been selectively established following an incipient wetness impregnation method, in which isolated Ni and Ce sites have been decorated onto a carbon–nitrogen support. The dual-atomic structure has been confirmed by systematic characterizations, including FT-EXAFS and AC HAADF-STEM measurements. This NiCe/CN DAC catalyst shows excellent reaction activities in both WGS and MSR, and it gives 6.5 $\mu mol_{H_2} g_{cat.}^{-1} s^{-1}$ of $H_2$ generation rate and only 0.8% CO selectivity at complete methanol conversion at 513 K, superior to $Ni/CeO_2$ and a series of noble-metal catalysts compared. The promoted reaction performance was tentatively attributed to the DAC structure and detailed electronic modification from isolated Ce to the adjacent Ni following quasi-in situ XPS analysis. In addition, systematic kinetic studies and SSITKA investigations suggest that the MD and WGS occurred on independent active sites. It is probable that $CH_3OH$ was mainly dissociatively adsorbed on the Ni surface to form $CH_3O^*$, and was followed by subsequent dehydrogenation to create $CO^*$. The rupture of the C–H bond within $CH_3O^*$ was assumed to be the KRS for the MD reaction. The $O_V$ over $CeO_x$ was assumed to be the main active component in the activation of $H_2O$ with the rupture of $O_L$–H as the KRS for the WGS reaction, which would not be highly involved in the hydrogen production under differential conditions, while it would be very important to determine the reaction selectivities once the methanol conversion promoted. All of these assumptions were further confirmed by a series of KIE analyses. This atomic $Ni$–$CeO_x$ interfacial site does facilitate WGS and MSR reactions, and this work paves the way for rational active site design from atomic level.

## Experimental

### Synthetic procedures

For the synthesis of NiCe/CN DAC, 21.6 g urea (American Chemical Society (ACS), Aladdin) was first dissolved in 20 ml ultrapure water. Then, 0.48 mmol $Ni(NO_3)_2 \cdot 6H_2O$ (Analytical Reagent (AR), Aladdin) and 0.48 mmol $Ce(NO_3)_3 \cdot 6H_2O$ (AR, Aladdin) were independently dissolved in the solution. After stirring for minutes, some pieces of melamine sponges were put into the solution and stirred for 70 min at room temperature. The sponges were taken out into a 50 ml centrifugal pipe, then rapidly frozen by liquid nitrogen. Subsequently, the samples were dried through vacuum freeze-drying and calcined in a tube furnace at 823 K under $N_2$ for 4 h. The synthesis process of Ni/CN, Ce/CN, NiLa/CN and NiY/CN were similar to that of NiCe/CN with different metal precursors added. For the synthesis of Ni/CN and Ce/CN, only 0.48 mmol $Ni(NO_3)_2 \cdot 6H_2O$ or 0.48 mmol $Ce(NO_3)_3 \cdot 6H_2O$ were applied, respectively. For NiLa/CN or NiY/CN, $Ce(NO_3)_3 \cdot 6H_2O$ was replaced by $La(NO_3)_3 \cdot 6H_2O$ (AR, Aladdin) or $Y(NO_3)_3 \cdot 6H_2O$ (AR, Aladdin), respectively. The catalysts with different Ni loadings were synthesized with various amounts of $Ni(NO_3)_2 \cdot 6H_2O$ added (0.022 mmol for 0.1% NiCe/CN DAC, 0.109 mmol for 0.5% NiCe/CN DAC, 0.218 mmol for 1% NiCe/CN DAC and 0.654 mmol for 3% NiCe/CN DAC, respectively), while the same amount of $Ce(NO_3)_3 \cdot 6H_2O$ (0.48 mmol) was used.[53]

### Characterizations

The morphologies of the as-received sample were characterized by TEM on a JEM-2800 microscope (JEOL, Japan), operating at an acceleration voltage of 200 kV. The fresh NiCe/CN DAC

sample and sample after reaction were suspended in ethanol by ultra-sonication, and the suspension was then dropped onto the copper grid for TEM characterizations.

The crystalline structures of the as-obtained samples were tested by XRD on a Rigaku Smart-lab X-ray diffractometer (Rigaku, Japan) with Cu Kα radiation ($\lambda$ = 1.5406 Å, 20 mA and 40 kV).

N$_2$ adsorption–desorption isotherms were obtained on Micromeritics APSP 2460 at 77 K, and Brunauer–Emmett–Teller (BET) method was used to calculate the surface area.

The element content was measured by inductively coupled plasma optical emission spectrometry (ICP-OES: Thermo Fisher iCAP PRO).

The thermogravimetric analysis of the NiCe/CN DAC sample after the reaction was carried out on a thermogravimetric analyzer (TGA 55). The sample was heated from room temperature to 1097 K at 10 K min$^{-1}$ under the flow of N$_2$ (40 mL min$^{-1}$).

AC HAADF-STEM images were taken at 300 kV on a FEI-Titan Cubed Themis G2 300 scanning transmission electron microscope. The fresh NiCe/CN DAC sample was suspended in ethanol by ultra-sonication, and the suspension was then dropped onto the microgrids for AC HAADF-STEM characterization.

The atom size distribution was measured from the AC HAADF-STEM image, and nanoparticle size distribution was measured from the TEM image. The diameter ($\langle d \rangle$) was calculated using the following equation:

$$\langle d \rangle (\mathrm{nm}) = \frac{\sum n_i d_i^3}{\sum n_i d_i^2} \qquad (5)$$

where $n_i$ is the number of atoms or clusters with a diameter $d_i$ from >100 atoms or clusters.

The XAS characterizations (including XANES and EXAFS) were recorded at the Singapore Synchrotron Light Source (SSLS) center, where a pair of channel-cut Si(111) crystals were utilized in the monochromator. The storage ring was working at 2.5 GeV with an averaged electron current of <200 mA. The acquired EXAFS results were extracted and processed according to the standard procedures with the ATHENA module implemented in the FEFIT software packages. The $k^3$-weighted Fourier transform (FT) of $x(k)$ in $R$ space was obtained within the range of 0 to 14.0 Å by applying a Besse window function, and the prepared catalysts were not pre-treated prior to this characterization.

The change of the chemical state of the metal species on NiCe/CN DAC, Ni/CN SAC and Ni/CeO$_2$ during the MSR was analyzed through the quasi-*in situ* XPS experiments, accomplished on a Thermo Scientific ESCALAB 250Xi photoelectron spectrometer equipped with a monochromatic microfocused Al-Kα X-ray source (1486.8 eV). Firstly, the catalyst was pressed into a small tablet and transferred into the pretreatment chamber, and activated under flowing 10 vol% H$_2$/Ar (total flow rate: 50 mL min$^{-1}$) at 623 K for 2 h. The activated sample was then cooled to room temperature and transferred directly into the chamber for XPS measurement without exposure to air. Then activated catalyst was diverted back to the pretreatment

chamber and treated at 623 K under the flow of methanol steam (1 kPa CH$_3$OH, Ar balanced, total flow rate: 30 mL min$^{-1}$) for 1 h. After treatment, the catalyst was switched back to the chamber for XPS analysis at room temperature without exposure to air. At last, the above process was repeated and we introduced the methanol/water steam into the pretreatment chamber at 623 K for 1 h (1 kPa CH$_3$OH, 16.02 kPa H$_2$O, Ar balanced, total flow rate: 30 mL min$^{-1}$), after which the final chemical state of the sample was determined (XPS analysis at room temperature).

### Catalytic performance measurement

MSR and WGS reactions were performed in a continuous plug-flow reactor. In a typical catalytic measurement, 100 mg of catalysts were placed in the vertical quartz tube (i.d. 1 cm) mixed mechanically with 400 mg silica (Sigma Aldrich) and sandwiched by quartz wool. The temperatures of the transfer line and catalyst bed were controlled by the temperature controller (UDLAN, 516P) equipped with a K-type thermocouple, which was placed in the constant temperature area of the reactor and closed to the catalyst bed to monitor the reaction temperature. Flow rates of gases were conducted by mass flow controllers (MFC Sevenstar, D07). Liquid reactants (CH$_3$OH, Saifuri, >99.9%; H$_2$O, NJDULY) were fed by the syringe pumps (Longer, LSP01-1BH). Before the reaction, all catalysts were firstly pre-treated in flowing 10 vol% H$_2$/Ar (total flow rate: 100 mL min$^{-1}$) at 623 K for 2 h. As for MSR, a mixture of 10 wt% CH$_3$OH/H$_2$O was introduced to the evaporator by a syringe pump and carried to the catalyst bed by co-feeding Ar (1 kPa CH$_3$OH, 16.02 kPa H$_2$O, Ar balanced, total flow rate: 30 mL min$^{-1}$), heated from 423 K to 623 K and the ramping rate was 10 K min$^{-1}$. For WGS, Ar and CO were mixed and fed to the reactor regulated by mass flow controllers along with flowing water (2 kPa CO, 10 kPa H$_2$O, Ar balanced, total flow rate: 80 mL min$^{-1}$). The products were analyzed online by gas chromatography (GC-2014, Shimadzu) equipped with a flame ionization detector (FID, connected to an Rtx-1 capillary column) and a thermal conductivity detector (TCD, connected to MS-13x and Porapak-S columns), respectively. Conversion and product selectivity could be calculated by peak area from GC.

The conversion of methanol (Conv.$_{CH_3OH}$) was calculated according to the equation, as follows:

$$\mathrm{Conv.}_{CH_3OH}(\%) = \frac{n_{CH_4} + n_{CO} + n_{CO_2}}{n_{CH_4} + n_{CO} + n_{CO_2} + n_{CH_3OH}} \times 100\% \quad (6)$$

The selectivities of products were calculated according to the equation, as follows:

$$\mathrm{Selec.}_{CO}(\%) = \frac{n_{CO}}{n_{CH_4} + n_{CO} + n_{CO_2}} \times 100\% \qquad (7)$$

$$\mathrm{Selec.}_{CO_2}(\%) = \frac{n_{CO_2}}{n_{CH_4} + n_{CO} + n_{CO_2}} \times 100\% \qquad (8)$$

$$\mathrm{Selec.}_{CH_4}(\%) = \frac{n_{CH_4}}{n_{CH_4} + n_{CO} + n_{CO_2}} \times 100\% \qquad (9)$$

The conversion of CO (Conv.$_{CO}$) was estimated according to the equation, as follows:

$$\text{Conv.}_{CO}(\%) = \frac{n_{CO_2}}{n_{CO} + n_{CO_2}} \times 100\% \qquad (10)$$

The turnover rate of mmol $H_2$ product yield per second per gram catalyst was calculated according to the equation, as follows:

$$\text{TOR}\left(\mu\text{mol}_{H_2} \text{ g}_{cat.}^{-1} \text{ s}^{-1}\right) = \frac{n_{H_2}}{m_{cat.} \times t} \qquad (11)$$

**Steady-state isotopic transient kinetic analysis (SSITKA) combined with *in situ* FTIR measurements**

SSITKA experiments were performed on the gas–solid transient reactor, equipped with two separate gas lines to control the labeled and unlabeled gas mixtures, respectively, and a four-way valve to ensure the quick switch of feed streams ($<200$ ms, steady-state was reached before switching). The reaction system was maintained in the absence of isotopic mass effect. The *in situ* FTIR measurements were performed on the spectrometer (BRUKER Tensor II) equipped with an MCT detector operated at atmospheric pressure. NiCe/CN DAC was pressed into self-supported wafer firstly, and then placed in the chamber and reduced at 623 K (heating ramp of 10 K min$^{-1}$) for 1 h with 3 vol% $H_2$/Ar. After purging by flowing Ar (50 mL min$^{-1}$), the IR spectra were recorded once the 2 kPa $CH_3OH$ (Ar balanced, total flow rate: 50 mL min$^{-1}$) was introduced to the chamber by a syringe pump (Longer, TJ-3A/W0109-1B). This condition was held for 50 min to reach a steady-state. Background spectra were recorded under this condition, and then the unlabeled reactant was switched to labeled reactant mixtures (*e.g.*, 2 kPa $CD_3OD$, Ar balanced, total flow rate: 50 mL min$^{-1}$) for 50 min. The infrared spectra were continuously collected during this process. The IR spectra were recorded with the instrument resolution set at 4 cm$^{-1}$, and 32 scans were applied and averaged for each spectrum. Isotope exchange experiments of water (10 kPa $H_2O$ was switched to 10 kPa $D_2O$, Ar balanced, total flow rate: 100 mL min$^{-1}$) and methanol with different pressures of water co-fed (2 kPa $CH_3OH$ + 10 kPa $H_2O$ was switched to 2 kPa $CD_3OD$ + 10 kPa $H_2O$, 2 kPa $CH_3OH$ + 15 kPa $H_2O$ was switched to 2 kPa $CD_3OD$ + 15 kPa $H_2O$, Ar balanced, total flow rate: 50 mL min$^{-1}$) were carried out following the same procedure described above, but instead of recording the initial unlabeled reactant as background, the background was recorded after purging by flowing Ar.

The residual coverage ($\Theta_{des}$) of surface species at time t was estimated by the equation below:

$$\Theta_{des} = \sum_{i=1}^{n} x_i k_i e^{-k_i t} \qquad (12)$$

where $x_i$ represents the steady-state fractional amount of the surface species at the ith active site, $k_i$ represents the desorption constant of the species from each active site, and $n$ represents the number of active sites.

**Isotope tracing and kinetic isotope effects assessment**

The kinetic isotope effects (KIEs) of MD, WGS and MSR on $H_2$ formation were measured over 1% NiCe/CN DAC under steady-state conditions.

As for MSR, $CH_3OH$ was replaced stepwise by $CH_3OD$ and $CD_3OD$, while keeping the pressure of $H_2O$ constant (2 kPa $H_2O$). Furthermore, $H_2O$ was replaced by $D_2O$ with the pressure of $CD_3OD$ remaining constant (1 kPa $CD_3OD$). Finally, the reaction was switched to $CD_3OD$ + $H_2O$, $CD_3OD$ + $H_2O$, and $CH_3OH$ + $H_2O$ sequentially to estimate the deactivation during the measurements (1 kPa isotopes of $CH_3OH$, 2 kPa isotopes of $H_2O$, Ar balanced, 623 K, GHSV = 19 099 h$^{-1}$).

As for MD, $CH_3OH$ was replaced stepwise by $CH_3OD$ and $CD_3OD$, and then returned to $CH_3OD$ and $CH_3OH$ with the pressure maintained at 1 kPa to estimate the deactivation during the measurements (1 kPa isotopes of $CH_3OH$, Ar balanced, 623 K, GHSV = 19 099 h$^{-1}$).

As for WGS, $H_2O$ was initially replaced by $D_2O$, and then switched to $H_2O$ with the CO pressure maintained at 2 kPa to estimate the catalytic deactivation (2 kPa CO, 10 kPa isotopes of $H_2O$, Ar balanced, 623 K, GHSV = 19 099 h$^{-1}$).

## Author contributions

Y. H. and Z. L. contributed equally to this work. Y. Z., H. Z. and Y. D. designed the research, Z. L. performed the materials preparation, HAADF-STEM and XAFS characterizations, Y. H. performed the kinetic studies, quasi-*in situ* XPS analysis and the SSITKA characterizations. All of the authors participated in the discussion of the results and the writing of the manuscript.

## Conflicts of interest

There are no conflicts to declare.

## Acknowledgements

# References

1 K. Kumar, P. Daw and D. Milstein, *Chem. Rev.*, 2022, **122**, 385–441.

2 P. Preuster, C. Papp and P. Wasserscheid, *Acc. Chem. Res.*, 2017, **50**, 74–85.

3 G. A. Olah, *Angew. Chem., Int. Ed.*, 2005, **44**, 2636–2639.

4 G. A. Olah, G. K. S. Prakash and A. Goeppert, *J. Am. Chem. Soc.*, 2011, **133**, 12881–12898.

5 K. Sordakis, C. Tang, L. K. Vogt, H. Junge, P. J. Dyson, M. Beller and G. Laurenczy, *Chem. Rev.*, 2018, **118**, 372–433.

6 D. R. Palo, R. A. Dagle and J. D. Holladay, *Chem. Rev.*, 2007, **107**, 3992–4021.

7 E. Alberico and M. Nielsen, *Chem. Commun.*, 2015, **51**, 6714–6725.

8 J. Kothandaraman, S. Kar, A. Goeppert, R. Sen and G. K. S. Prakash, *Top. Catal.*, 2018, **61**, 542–559.

9 D. Li, X. Y. Li and J. L. Gong, *Chem. Rev.*, 2016, **116**, 11529–11653.

10 L. Chen, Z. Y. Qi, X. X. Peng, J. L. Chen, C. W. Pao, X. B. Zhang, C. C. Dun, M. Young, D. Prendergast, J. J. Urban, J. H. Guo, G. A. Somorjai and J. Su, *J. Am. Chem. Soc.*, 2021, **143**, 12074–12081.

11 L. Lin, W. Zhou, R. Gao, S. Yao, X. Zhang, W. Xu, S. Zheng, Z. Jiang, Q. Yu, Y. W. Li and C. Shi, *Nature*, 2017, **544**, 80–83.

12 B. A. Peppley, J. C. Amphlett, L. M. Kearns and R. F. Mann, *Appl. Catal., A*, 1999, **179**, 21–29.

13 B. A. Peppley, J. C. Amphlett, L. M. Kearns and R. F. Mann, *Appl. Catal., A*, 1999, **179**, 31–49.

14 D. K. Kim and E. Iglesia, *J. Phys. Chem. C*, 2008, **112**, 17235–17243.

15 B. Frank, F. C. Jentoft, H. Soerijanto, J. Krohnert, R. Schlogl and R. Schomacker, *J. Catal.*, 2007, **246**, 177–192.

16 C. J. Jiang, D. L. Trimm, M. S. Wainwright and N. W. Cant, *Appl. Catal., A*, 1993, **97**, 145–158.

17 K. Ploner, M. Watschinger, P. D. K. Nezhad, T. Gotsch, L. Schlicker, E. M. Kock, A. Gurlo, A. Gili, A. Doran, L. Zhang, N. Kowitsch, M. Armbruster, S. Vanicek, W. Wallisch, C. Thurner, B. Klotzer and S. Penner, *J. Catal.*, 2020, **391**, 497–512.

18 D. D. Li, F. Xu, X. Tang, S. Dai, T. C. Pu, X. L. Liu, P. F. Tian, F. Z. Xuan, Z. Xu, I. E. Wachs and M. H. Zhu, *Nat. Catal.*, 2022, **5**, 99–108.

19 S. Lin, D. Xie and H. Guo, *ACS Catal.*, 2011, **1**, 1263–1271.

20 S. Lin, R. S. Johnson, G. K. Smith, D. Xie and H. Guo, *Phys. Chem. Chem. Phys.*, 2011, **13**, 9622–9631.

21 N. Köwitsch, L. Thoni, B. Klemmed, A. Benad, P. Paciok, M. Heggen, I. Köwitsch, M. Mehring, A. Eychmüller and M. Armbrüster, *ACS Catal.*, 2021, **11**, 304–312.

22 K. Xu, C. Ma, H. Yan, H. Gu, W. W. Wang, S. Q. Li, Q. L. Meng, W. P. Shao, G. H. Ding, F. R. Wang and C. J. Jia, *Nat. Commun.*, 2022, **13**, 2443.

23 M. Cargnello, N. L. Wieder, T. Montini, R. J. Gorte and P. Fornasiero, *J. Am. Chem. Soc.*, 2010, **132**, 1402–1409.

24 M. Friedrich, S. Penner, M. Heggen and M. Armbruster, *Angew. Chem., Int. Ed.*, 2013, **52**, 4389–4392.

25 K. Fottinger, J. A. V. Bokhoven, M. Nachtegaal and G. Rupprechter, *J. Phys. Chem. Lett.*, 2011, **2**, 428–433.

26 M. Xu, S. Y. Yao, D. M. Rao, Y. M. Niu, N. Liu, M. Peng, P. Zhai, Y. Man, L. R. Zheng, B. Wang, B. S. Zhang, D. Ma and M. Wei, *J. Am. Chem. Soc.*, 2018, **140**, 11241–11251.

27 Y. R. Wang, J. M. Ma, X. Y. Wang, Z. S. Zhang, J. H. Zhao, J. Yan, Y. P. Du, H. B. Zhang and D. Ma, *ACS Catal.*, 2021, **11**, 11820–11830.

28 X. Y. Wang, D. D. Li, Z. R. Gao, Y. Guo, H. B. Zhang and D. Ma, *J. Am. Chem. Soc.*, 2023, **145**, 905–918.

29 S. K. Kaiser, Z. Chen, D. F. Akl, S. Mitchell and J. Pérez-Ramírez, *Chem. Rev.*, 2020, **120**, 11703–11809.

30 S. Y. Yao, X. Zhang, W. Zhou, R. Gao, W. Q. Xu, Y. F. Ye, L. L. Lin, X. D. Wen, P. Liu, B. B. Chen, C. Ethan, J. H. Guo, Z. J. Zuo, W. Z. Li, J. L. Xie, L. Lu, J. K. Christopher, L. Gu, C. Shi, A. R. Jose and D. Ma, *Science*, 2017, **357**, 389–393.

31 X. Zhang, M. Zhang, Y. Deng, M. Xu, L. Artiglia, W. Wen, R. Gao, B. Chen, S. Yao, X. Zhang, M. Peng, J. Yan, A. Li, Z. Jiang, X. Gao, S. Cao, C. Yang, A. J. Kropf, J. Shi, J. Xie, M. Bi, J. A. van Bokhoven, Y. Li, X. Wen, M. Flytzani-Stephanopoulos, C. Shi, W. Zhou and D. Ma, *Nature*, 2021, **589**, 396–401.

32 L. Lin, Q. Yu, M. Peng, A. Li, S. Yao, S. Tian, X. Liu, A. Li, Z. Jiang, R. Gao, X. D. Han, Y. W. Li, X. D. Wen, W. Zhou and D. Ma, *J. Am. Chem. Soc.*, 2021, **143**, 309–317.

33 C. Mateos-Pedreroa, C. Azenha, D. A. P. Tanaka, J. M. Sousa and A. Mendes, *Appl. Catal., B*, 2020, **277**, 119243.

34 F. Bossola, T. Roongcharoen, M. Coduri, C. Evangelisti, F. Somodi, L. Sementa, A. Fortunelli and V. Dal Santo, *Appl. Catal., B*, 2021, **297**, 120398.

35 H. J. Xi, X. N. Hou, Y. J. Liu, S. J. Qing and Z. X. Gao, *Angew. Chem., Int. Ed.*, 2014, **53**, 11886–11889.

36 X. H. Xu, K. P. Shuai and B. Xu, *Catalysts*, 2017, **7**(6), 183.

37 H. Zhang, J. M. Sun, V. L. Dagle, B. Halevi, A. K. Datye and Y. Wang, *ACS Catal.*, 2014, **4**, 2379–2386.

38 L. N. Chen, K. P. Hou, Y. S. Liu, Z. Y. Qi, Q. Zheng, Y. H. Lu, J. Y. Chen, J. L. Chen, C. W. Pao, S. B. Wang, Y. B. Li, S. H. Xie, F. D. Liu, D. Prendergast, L. E. Klebanoff, V. Stavila, M. D. Allendorf, J. H. Guo, L. S. Zheng, J. Su and G. A. Somorjai, *J. Am. Chem. Soc.*, 2019, **141**, 17995–17999.

39 S. Zhang, Y. X. Liu, M. K. Zhang, Y. Y. Ma, J. Hu and Y. Q. Qu, *Nat. Commun.*, 2022, **13**, 5527.

40 P. Hu, Y. Diskin-Posner, Y. Ben-David and D. Milstein, *ACS Catal.*, 2014, **4**, 2649–2652.

41 S. Li and J. Gong, *Chem. Soc. Rev.*, 2014, **43**, 7245–7256.

42 H. Tian, X. Li, L. Zeng and J. L. Gong, *ACS Catal.*, 2015, **5**, 4959–4977.

43 H. Tian, C. L. Pei, Y. Wu, S. Chen, Z. J. Zhao and J. L. Gong, *Appl. Catal., B*, 2021, **293**, 120178.

44 A. H. Braga, D. C. de Oliveira, A. R. Taschin, J. B. O. Santos, J. M. R. Gallo and J. M. C. Bueno, *ACS Catal.*, 2021, **11**, 2047–2061.

45 Y. S. Wang, C. S. Wang, M. Q. Chen, J. X. Hu, Z. Y. Tang, D. F. Liang, W. Cheng, Z. L. Yang, J. Wang and H. Zhang, *Fuel*, 2020, **279**, 118449.

46  S. Chen, C. L. Pei and J. L. Gong, *Energy Environ. Sci.*, 2019, **12**, 3473.

47  G. W. Wu, C. X. Zhang, S. R. Li, Z. Q. Huang, S. L. Yan, S. P. Wang, X. B. Ma and J. L. Gong, *Energy Environ. Sci.*, 2012, **5**, 8942.

48  T. Wang, H. Y. Ma, L. Zeng, D. Li, H. Tian, S. N. Xiao and J. L. Gong, *Nanoscale*, 2016, **8**, 10177.

49  M. Q. Chen, D. F. Liang, Y. S. Wang, C. S. Wang, Z. Y. Tang, C. Li, J. X. Hu, W. Cheng, Z. L. Yang, H. Zhang and J. Wang, *Int. J. Hydrogen Energy*, 2021, **46**, 21796–21811.

50  Y. S. Wang, D. F. Liang, C. S. Wang, M. Q. Chen, Z. Y. Tang, J. X. Hu, Z. L. Yang, H. Zhang, J. Wang and S. M. Liu, *Renewable Energy*, 2020, **160**, 597–611.

51  C. S. Wang, Y. S. Wang, M. Q. Chen, J. X. Hu, Z. L. Yang, H. Zhang, J. Wang and S. M. Liu, *Int. J. Hydrogen Energy*, 2019, **44**, 26888–26904.

52  L. P. Song, Z. Liang, M. Z. Sun, H. B. Long and D. Y. Ping., *Energy Environ. Sci.*, 2022, **15**, 3494.

53  Z. Liang, L. P. Song, M. Z. Sun, H. B. Long and D. Y. Ping, *Sci. Adv.*, 2021, **7**, eabl4915.

54  L. L. Han, H. Cheng, W. Liu, H. Q. Li, P. F. Ou, R. Q. Lin, H. T. Wang, C. W. Pao, A. R. Head, C. H. Wang, X. Tong, C. J. Sun, W. F. Pong, J. Luo, J. C. Zheng and H. L. Xin, *Nat. Mater.*, 2022, **21**, 681–688.

55  L. L. Yin, S. Zhang, M. Z. Sun, S. Y. Wang, B. L. Huang and Y. P. Du, *Adv. Mater.*, 2023, **35**, 230248.

56  M. Han, N. Wang, B. Zhang, Y. J. Xia, J. Li, J. R. Han, K. L. Yao, C. C. Gao, C. N. He, Y. C. Liu, Z. M. Wang, A. Seifitokaldani, X. H. Sun and H. Y. Liang, *ACS Catal.*, 2020, **10**, 9725–9734.

57  Y. Xie, J. J. Chen, X. Wu, J. J. Wen, R. Zhao, Z. L. Li, G. C. Tian, Q. L. Zhang, P. Ning and J. M. Hao, *ACS Catal.*, 2022, **12**, 10587–10602.

58  M. Romeo, K. Bak, J. El Fallah, F. Le Normand and L. Hilaire, *Surf. Interface Anal.*, 1993, **20**, 508–512.

59  K. Ploner, M. Watschinger, P. D. K. Nezhad, T. Götsch, L. Schlicker, E. M. Köck, A. Gurlo, A. Gili, A. Doran, L. Zhang, N. Köwitsch, M. Armbrüster, S. Vanicek, W. Wallisch, C. Thurner, B. Klötzer and S. Penner, *J. Catal.*, 2020, **391**, 497–512.

60  J. S. Huberty and R. J. Madix, *Surf. Sci.*, 1996, **360**, 144–156.

61  A. Rezvani, A. M. Abdel-Mageed, T. Ishida, T. Murayama, M. Parlinska-Wojtan and R. J. Behm, *ACS Catal.*, 2020, **10**, 3580–3594.

62  R. C. Millikan and K. S. Pitzer, *J. Am. Chem. Soc.*, 1958, **80**, 3515–3521.

63  S. L. Shannon and J. G. Goodwin Jr, *Chem. Rev.*, 1995, **95**, 677–695.

64  R. J. Madon and M. Boudart, *Ind. Eng. Chem. Fundam.*, 1982, **21**, 438–447.

65  A. A. Peterson and J. K. Nørskov, *J. Phys. Chem. Lett.*, 2012, **3**, 251–258.

66  F. Solymosi and A. Berkó, *J. Catal.*, 1986, **101**, 458–472.

67  G. Wang, X. L. Jiang, Y. F. Jiang, Y. G. Wang and J. Li, *ACS Catal.*, 2023, **13**, 8413–8422.

68  M. Gomez-Gallego and M. A. Sierra, *Chem. Rev.*, 2011, **111**, 4857–4963.